frontiers | Frontiers in Electronic Materials

TYPE Original Research
PUBLISHED 08 March 2024
DOI 10.3389/femat.2024.1339293



OPEN ACCESS

EDITED BY
Tsuyoshi Tajima,
Los Alamos National Laboratory (DOE),
United States

REVIEWED BY
Claire Antoine,
Université Paris-Saclay, France
Fang Yuan,
Princeton University, United States
Mohammed Fouaidy,
UMR9012 Laboratoire de Physique des 2 Infinis Irène Joliot-Curie (IJCLab), France

*CORRESPONDENCE
G. Ciovati,
gciovati@jlab.org

RECEIVED 15 November 2023
ACCEPTED 20 February 2024
PUBLISHED 08 March 2024

CITATION
Parajuli I, Ciovati G and Gurevich A (2024), Magneto-thermal limitations in superconducting cavities at high radio-frequency fields.
*Front. Electron. Mater.* 4:1339293.
doi: 10.3389/femat.2024.1339293



# Magneto-thermal limitations in superconducting cavities at high radio-frequency fields

I. Parajuli[1], G. Ciovati[1,2]* and A. Gurevich[1]

[1]Center for Accelerator Science, Department of Physics, Old Dominion University, Norfolk, VA, United States, [2]Thomas Jefferson National Accelerator Facility, Newport News, VA, United States

The performance of superconducting radio-frequency Nb cavities at high radio-frequency (rf) fields in the absence of field emission can be limited by either a sharp decrease of the quality factor $Q_0(B_p)$ above peak surface magnetic fields $B_p$ ~100 mT or by a quench. We have measured $Q_0(B_p)$ at 2 K of several 1.3 GHz single-cell Nb cavities with different grain sizes, and with different ambient magnetic fields and cooldown rates below the critical temperature. Temperature mapping and a novel magnetic field mapping systems were used to find the location of "hot-spots" and regions of trapped magnetic flux. The use of a variable input coupler allowed further exploring the dissipative state. The results showed a remarkable thermal stability in some cavities with up to 200 W of rf power dissipation at 2 K, whereas other cavities quenched at much lower rf power. We observed a narrow distributions of the onset fields of hot-spots which were not affected by thermal cycling or by conditions which favor the formation of Nb hydrides. Furthermore, a poor correlation was found between the location of hot-spots and trapped vortices. We suggest that the totality of our experimental data can be explained by a sharp increase of the residual surface resistance above 120–140 mT due to the field-induced breakdown of a proximity-coupled metallic suboxide layer at the surface.

KEYWORDS

**radiofrequency, niobium, superconducting RF cavities, particle accelerators, surface resistance (Rs), nonlinear rf losses**

## 1 Introduction

The performance of superconducting radio-frequency (SRF) Nb cavities has been improving over the past decades, both in terms of the maximum accelerating gradient and the maximum quality factor, making them one of the building blocks or modern particle accelerators. In the absence of extrinsic effects such as field emission or multipacting, the performance of Nb cavities at high peak radio-frequency (rf) surface magnetic field, $B_p >$ 100 mT is limited by either a sharp decrease of the quality factor $Q_0(B_p)$, leading to an unacceptably high cryogenic heat load, and referred to in the literature as "high-field Q-slope" (HFQS), or by a sudden breakdown of superconductivity, referred to as "quench" (Padamsee, 2001).

The origin of the HFQS has been the subject of numerous studies for more than 20 years. Some of the most popular models attribute the HFQS to the presence of impurities, defects or nano-precipitates within the rf penetration depth or losses related to the native oxide layer (Halbritter, 1978; Visentin, 2003; Ciovati, 2006a; Ciovati, 2006b; Visentin, 2006; Ciovati et al., 2010; Weingarten, 2011; Romanenko et al., 2013a). Empirically, it has been found that a low-temperature baking (LTB) of the cavities at ~ 120°C for 3–48 h increases

both the quality factor and the maximum accelerating gradient, eliminating the HFQS (Visentin et al., 1999; Ciovati, 2004; Ciovati et al., 2007; Romanenko et al., 2013b; Ciovati et al., 2018; Charrier et al., 2019). Temperature mapping investigations of cavities at or below 2 K have shown that the HFQS correlates with a broad, non-uniform heating of the inner surface at high rf fields (Eremeev and Padamsee, 2006; Ciovati et al., 2007; Eremeev et al., 2013). The regions of enhanced rf dissipation on the cavity surface are commonly referred to as "hotspots". RF measurements on cavities with different distributions of surface electric and magnetic fields indicate that the HFQS is primarily driven by the surface magnetic field rather than overheating (Ciovati, 2005; Ciovati and Kneisel, 2006).

It has been shown experimentally, that the origin of quenches in SRF cavities can be either "magnetic" or "thermal" (Padamsee et al., 1981; Eremeev and Palczewski, 2014). Magnetic field quenches have been associated with the presence of topographic defects on the inner surface causing a local magnetic field enhancement (Xie and Liepe, 2013). Thermal quenches have been associated with the presence of normal-conducting defects at the inner surface causing excessive local heating (Shu et al., 1996). Another essential factor increasing the residual surface resistance and reducing the SRF breakdown field has been associated with trapped vortices which appear during cavity cooldown through $T_c$. Trapped vortices in such flux spots produce additional RF heating so that the flux spots also become hotspots which can be detected by temperature mapping (Padamsee, 2009). A distinctive feature of vortex hotspots is that they exhibit hysteretic behavior upon cycling the rf field and can be changed or moved by applying temperature gradients caused by either external heaters or laser beams (Ciovati and Gurevich, 2008; Gurevich and Ciovati, 2013). The amount of trapped magnetic flux in SRF cavities is reduced by magnetic shielding and by cooling them through $T_c$ with a high temperature gradient (Vogt et al., 2013; Romanenko et al., 2014; Huang et al., 2016; Posen et al., 2016). Optimizing cavity manufacturing and processing as well as the cavity cooling rate have significantly improved the SRF performance (Antoine, 2012; Posen et al., 2022). The highest peak surface magnetic fields in SRF cavities tested at 2 K are typically achieved by applying electropolishing (EP) and LTB as final surface treatments, resulting in $B_p > 120$ mT limited by quenching (Geng et al., 2011).

While the detrimental effects of trapped flux on the residual rf losses and the SRF breakdown field have been well-documented (Padamsee, 2009; Gurevich and Ciovati, 2013; Liarte et al., 2018), it remains unclear whether the HFQS is primarily driven by the trapped flux or microstructural materials defects. Understanding the mechanisms of the HFQS thus requires a combination of different experimental techniques which would allow us to separate the contributions of trapped vortices and materials defects to $Q_0(B_p)$ at high rf fields. This is a goal of this work in which we combine the rf measurements of $Q_0(B_p)$ on several Nb cavities which underwent different treatments, along with the temperature mapping and a recently developed magnetic mapping of the cavity surface using arrays of magnetic field sensors (Parajuli et al., 2022). This allows us not only to identify the SRF hostpots and magnetic flux spots but also to superimpose the temperature and magnetic maps to see any correlation between the hotspots and flux spots in the HFQS field region. Particularly, we investigate if the hotspots which show a sharp increase of the overheating at the onset of HFQS are also the magnetic flux spots exhibiting the hysteretic behavior upon cycling the rf field or changing the cooling rate near $T_c$, as characteristic of trapped vortices. The lack of such correlation would mean that the HFQS is primarily driven by SRF performance-limiting materials defects.

We present experimental results aiming at addressing the following outstanding questions: (i) does the HFQS "saturate" beyond a certain $B_p$-value? (ii) is the HFQS caused by hotspots and regions of trapped magnetic flux and are the hotspot locations reproducible with respect to repeated cool-down? (iii) is the HFQS impacted by holding the cavity at 90–150 K, which favors the formation of normal-conducting niobium hydrides? (iv) does the HFQS result in thermal quench? (v) what could be the mechanisms of HFQS? To answer these questions we measured $Q_0(B_p)$ of 1.3 GHz single-cell cavities at 2.0 K, using a variable input coupler antenna (Ciovati and Turlington, 2019). Temperature maps have been acquired during some of the high-power rf tests. Magnetic field maps have also been measured during some of the rf tests using a magnetic field scanning system described in Ref. (Parajuli et al., 2022).

The paper is organized as follows. In Section 2 we present the totality of our experimental data including $Q_0(B_p)$ measurements on cavities subjected to different treatments, temperature mapping revealing hotspots and distribution of local field onsets of HFQS and magnetic field mapping revealing flux spots of trapped vortices and their correlation with the hotspots and grain boundary structures. Section 3 contains discussion of our experimental data in light of different models of HFQS suggested in the literature followed by our thermal feedback model combined with a model of superconductivity breakdown in proximity-coupled suboxide layer, which captures the features of HFQS observed in this work. Section 4 finishes with conclusions.

## 2 Experimental results

The single-cell cavities used for this study were made from high-purity (residual resistivity ratio greater than 300) ≃ 3 mm thick Nb. Two of them, labeled N3 and PJ1-1 were made from large-grain (LG) Nb (Kneisel et al., 2015) disks from OTIC Ningxia, China. Other cavities labeled RTD-TD01, EZ-SSC-01, TE1G001 and TE1NS001 were made of standard fine-grain (FG) Nb from Tokyo-Denkai, Japan. N3 and PJ1-1 have the TESLA/XFEL center-cell shape with the geometry factor, $G$ = 269.8Ω, $B_p/E_{acc}$ = 4.12 mT/(MV/m), where $E_{acc}$ is the accelerating gradient. The other cavities have the TESLA/XFEL end-cell shape [$G$ = 277.8Ω, $B_p/E_{acc}$ = 4.23 mT/(MV/m)] (Aune et al., 2000).

Some of the cavities have a long processing history as they have been used for R&D projects on N-doping (RDT-TD01), flux expulsion (EZ-SSC-01), high-gradient and large-grain material (PJ1-1 and N3). The highest temperature the cavities have been annealed at in a vacuum furnace is listed in Table 1, along with the last chemical treatment prior to the rf tests conducted for this study. Cavities N3 and PJ1-1 have been etched by buffered chemical polishing (BCP) (HF:$HNO_3$:$H_3PO_4$ = 1:1:2 by volume, ~ 15 °C, ~ 1 μm/min removal rate), whereas the inner surface of the other cavities was polished by electropolishing (EP) ($H_2SO_4$:HF = 10:1 by

TABLE 1 Summary of the cavities rf performance at 2.0 K, along with the type of material, highest annealing temperature and time and last chemical process prior to the rf test.

| Cavity name | Nb material | Annealing | Treatment | $B_{p,max}$ (mT) | $Q_0(B_{p,max})$ | $P_c(B_{p,max})$ (W) | Limit |
|---|---|---|---|---|---|---|---|
| EZ-SSC-01 | FG | 800°C/2 h | 100 μm EP | 153 ± 8 | (8.0 ± 1.0) × $10^8$ | 200 ± 10 | Rf power |
| RDT-TD01 | FG | 900°C/3 h | 30 μm EP | 161 ± 8 | (1.2 ± 0.1) × $10^9$ | 153 ± 16 | Rf power |
| PJ1-1 | LG | 800°C/2 h | 5 μm BCP | 141 ± 7 | (7.5 ± 0.6) × $10^8$ | 180 ± 14 | Rf power |
| N3 | LG | 1250°C/3 h | 20 μm BCP | 142 ± 7 | (7.0 ± 0.5) × $10^8$ | 181 ± 16 | Quench |
| TE1G001 | FG | 800°C/2 h | 25 μm EP | 117 ± 6 | (1.1 ± 0.1) × $10^{10}$ | 8.7 ± 0.7 | Quench |
| TE1NS001 | FG | 900°C/3 h | 30 μm EP | 131 ± 6 | (1.2 ± 0.1) × $10^{10}$ | 10.2 ± 0.8 | Quench |

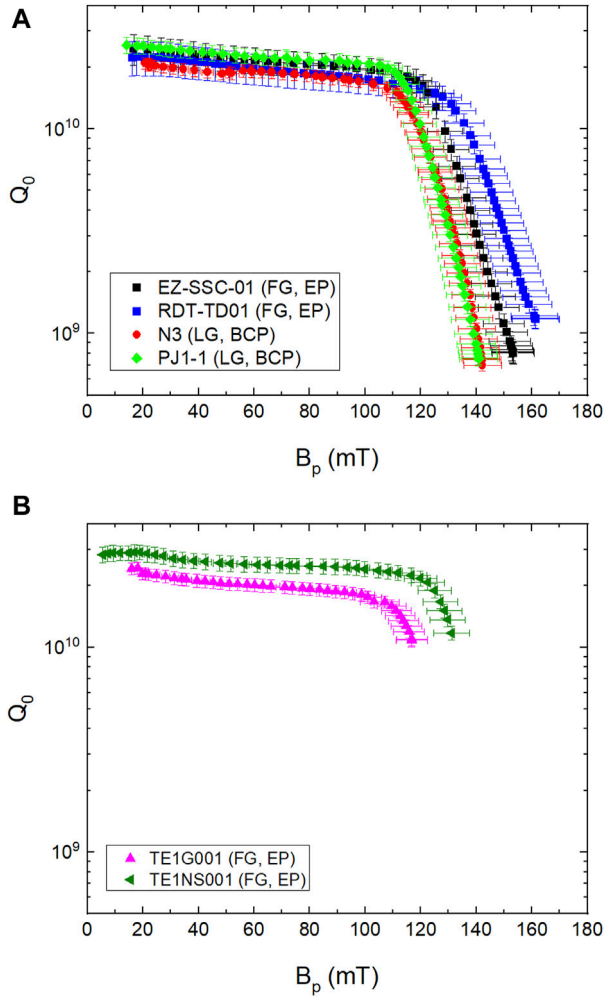


FIGURE 1
$Q_0(B_p)$ measured at 2.0 K for 1.3 GHz single-cell cavities limited by the HFQS **(A)** or by a premature quench **(B)**.

volume, ~ 13 V, ~ 0.3 μm/min removal rate, equator temperature kept at ~ 21 °C).

The final preparation prior to the rf test of each cavity consisted of a 30 min degreasing with a detergent diluted in ultra-pure water and with ultrasonic agitation, high-pressure (80 bar) rinsing with ultra-pure water for ~ 75 min, assembly of the pick-up antenna and of the variable input coupler antenna in an ISO 4 clean room, evacuation to ~ 1 × $10^{-8}$ mbar and He leak-check. The cavities were rf tested in a vertical cryostat, 41 cm in diameter, 275 cm deep, with a low residual magnetic field $B_a$ ~ 0.2 μT and cooled with liquid helium to 2 K, with a typical temperature gradient along the cavity axis $dT/dz$ ~ 0.4 K/cm at $T_c$.

A summary of the cavities rf performance at 2.0 K is given in Table 1; Figure 1 shows representative plots of $Q_0(B_p)$ for some of these cavities. For cavities TE1G001, TE1NS001 and N3, the maximum rf field was limited by a quench, whereas the other cavities were limited by the output power of the rf amplifier, ~ 350 W, used for the tests. No x-rays were detected in any of the tests, except for cavity EZ-SSC-01, for which a maximum dose rate of 4 mR/h with an onset of 152 mT close to the maximum field, was measured. Such low X-ray intensity is not expected to impact $Q_0$ significantly.

The variable input coupler was adjusted prior to measuring each data point, during each rf test, in order to maintain close to the critical coupling conditions, which maximize the fraction of forward power from the high-power amplifier into the cavity. The ratio of reflected power divided by the forward power at the maximum gradient was 25%, 1% and 0.3% for cavities RDT-TD01, PJ1-1 and EZ-SSC-01, respectively. The input antenna was not long enough to allow better coupling for RDT-TD01 at the highest field.

The power $P_c$ dissipated in the cavity at the highest field reached 150 W, 180 W and 200 W in cavities RTD-TD01, PJ1-1 and EZ-SSC-01, respectively. The cooling capacity of the plant supplying liquid helium at Jefferson Lab's Vertical Test Area is ~ 170 W at 2.0 K, therefore the He bath temperature increased to ~ 2.04 K at the highest field in cavities PJ1-1 and EZ-SSC-01. Details about the cryogenic facility at Jefferson Lab for the vertical test of SRF cavities can be found in Reece et al. (1991). In order to limit the boil-off of liquid He, the time interval between each data point was ~ 20 s at power levels above ~ 50 W. This is much longer then the cavity decay time but it is much shorter than the thermal time constant of the rf power cable.

## 2.1 Results of temperature mapping

As mentioned in Section 1, varying temperature gradients and residual dc magnetic field applied to SRF cavities being cooled below $T_c$ can impact their residual resistance: gradients exceeding 0.03 K/cm result in better expulsion of the magnetic flux (Vogt et al., 2013;

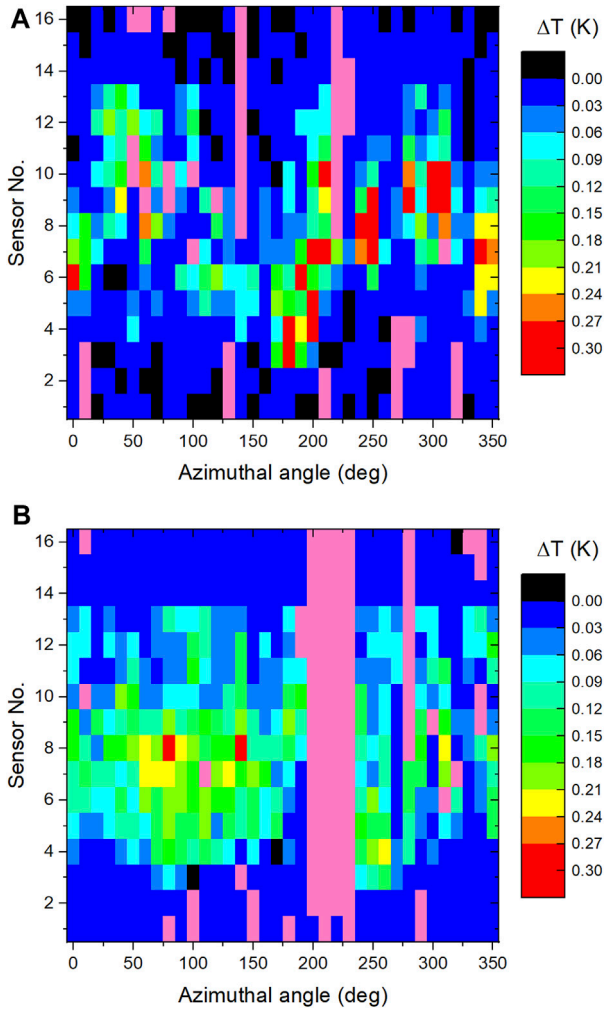


FIGURE 2
Unfolded temperature map at $B_p$ = 165 mT and at $B_p$ = 140 mT measured at 2.0 K during the baseline for cavities PJ1-1 **(A)** and RDT-TD01 **(B)**, respectively. Sensor 1 is at the top iris, sensor 16 is at the bottom beam tube, close to the iris. Sensor 8 is on the equator weld. Faulty channels/sensors are shown in pink in the color map.

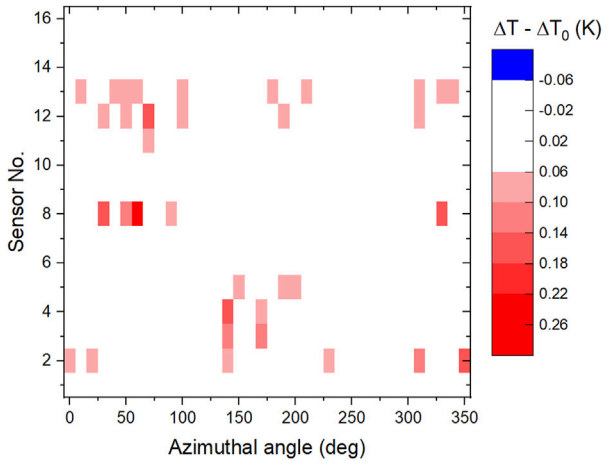


FIGURE 3
Difference between temperature maps at 2.0 K, 129 mT measured for cavity PJ1-1 after cool-down with low $dT/dz$ and high $B_a$ and during the baseline test (high $dT/dz$ and low $B_a$). The surface magnetic field is within 1% of the peak value in the region between sensors No. 4 and No. 12.

Romanenko et al., 2014; Huang et al., 2016; Posen et al., 2016). It was also shown that holding a Nb cavity at temperatures 90–150 K for several hours promotes the formation of lossy Nb hydrides, which also impact the residual resistance (Bonin et al., 1992; Knobloch, 2003). To reveal hotspots produced by bundles of trapped vortices and lossy precipitates, we performed cryogenic rf tests of cavities RDT-TD01 and PJ1-1 combined with the temperature mapping as an additional diagnostic tool. This enabled us to evaluate the impact of different cool-down rates, residual dc magnetic field and hydride formation on the intensity and distribution of the hotspots which may cause the HFQS. Detailed information about the values of $dT/dz$, the residual field $B_a$ and quench location for each of the rf tests discussed in this Section are listed in the Appendix, along with representative $Q_0(B_p)$ curves.

Our temperature mapping system consisted of an array of 576 carbon resistance temperature devices (RTDs) attached to the outer cavity surface. Apiezon N grease is applied between the sensors and the cavity to improve the thermal contact. Details about the temperature sensors' calibration, heat transfer efficiency and the temperature mapping system can be found in Refs. (Romijn et al., 1983; Knobloch et al., 1994; Knobloch, 1997; Ciovati, 2005). The setup was used to measure the temperature maps $\Delta T$ (**r**, $B_p$) = $T$ (**r**, $B_p$) − $T_0$ as a function of the rf field, where $T$ (**r**, $B_p$) is the local temperature of the cavity outer surface measured by each RTD and $T_0$ is the temperature of the He bath. To detect hotspots relative to the baseline, we adopted the following criterion: $|\Delta T - \Delta T_0| \geq \sigma_B \langle d\Delta T/dB_p \rangle$, where $\sigma_B \sim 0.06 B_p$ is the standard deviation of the $B_p$-measurement, and $\langle d\Delta T/dB_p \rangle$ is the average slope of $\Delta T$ ($B_p$) in a hotspot at the field $B_p$ at which the temperature map was measured. The value of $\langle d\Delta T/dB_p \rangle$ increases with $B_p$ beyond the onset of the HFQS, therefore the temperature maps measured at 129 mT were chosen for comparison of different tests. We observed $\langle d\Delta T/dB_p \rangle \sim$ 8 mK/mT at 129 mT and 146 mT for cavities PJ1-1 and RDT-TD01, respectively, compared to ~ 100 mK/mT at $B_{p,max}$. Following the above criteria, we identify a change in a temperature map as compared to the baseline if $|\Delta T - \Delta T_0| \geq$ 60 mK for at least one location.

The residual magnetic field was measured with three single-axis cryogenic flux-gate magnetometers (FGMs) distributed around the equator circumference, at a radial distance of ~ 8 cm. The axis of the FGMs was aligned to the cavity axis. The residual magnetic field, $B_a$, was changed by varying the current in a set of compensation coils wound around a cylindrical MuMetal® shield surrounding the cryostat.

The temperature gradient induced along the cavity during its cool-down was determined by two Cernox® RTDs mounted on the top beam tube and two mounted at the bottom beam tube, the distance between the two pairs being ~ 23.5 cm. The temperature gradient during cool-down was varied by adjusting the power to the heater at the bottom of the cryostat and the opening of the Joule-Thomson valve, which controls the inlet flow of cold He gas at the bottom of the cryostat. The typical cooling rate close to $T_c$ was ~ 2 K/min and ~ 0.1 K/min to achieve a high or low temperature gradient, respectively.

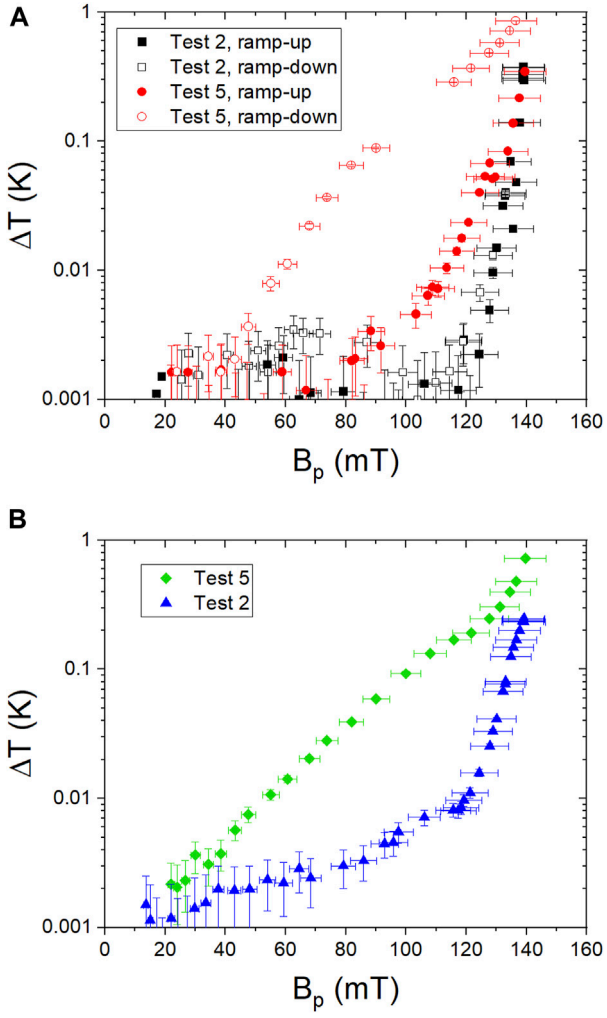


FIGURE 4
$\Delta T$ ($B_p$) for hot-spots at locations 200°/4 **(A)** and 60°/8 **(B)** of cavity PJ1-1 measured during Tests No. 2 (high $dT/dz$ and low $B_a$) and 5 (low $dT/dz$ and high $B_a$). Empty symbols in **(A)** represent data taken while decreasing the rf field, after quench. The data from a second ramp-up of the rf field in **(A)**, not shown for clarity, follow the empty symbols.

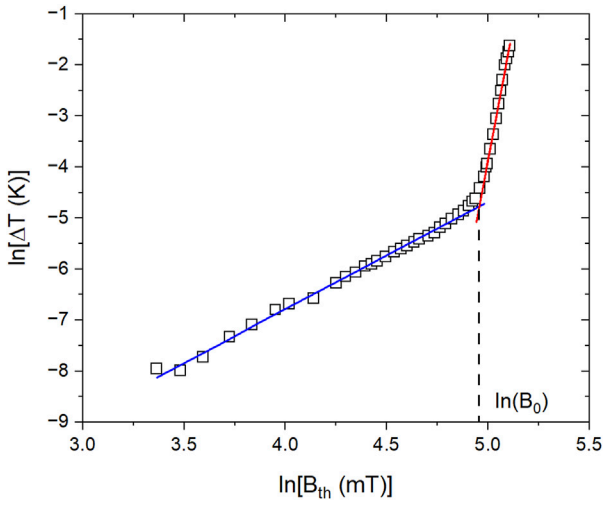


FIGURE 5
Hot-spot at location 90°/6 in the baseline test of cavity RDT-TD01 illustrating the method to determine the onset of the HFQS. Solid lines are least-squares linear fits to ln ($\Delta T$) vs. ln ($B_{th}$) at low and high rf field.

### 2.1.1 Impact of cool-down conditions

Figure 2 shows the "unfolded" temperature maps measured at 2.0 K just before quench for cavities PJ1-1 and RDT-TD01 during the baseline rf test, after cool-down with high $dT/dz$ = 3.5 K/cm and low $B_a$ = 0.8 $\mu$T to minimize any trapped flux. Significant overheating occurs in the equator area, being more diffused in the fine-grain cavity RDT-TD01 and with sharper hot-spots in the large-grain cavity PJ1-1, consistent with the findings of Ref. (Eremeev and Padamsee, 2006).

The HFQS T-map results from the rf tests following the baseline can be summarized as follows: (i) the T-maps were reproducible following similar cool-down conditions as for the baseline; (ii) the T-maps did not change after cool-down with low $B_a$ and low $dT/dz$; (iii) the T-maps did not change after holding the cavities between 90–160 K. Changes in temperature maps compared to the baseline test occurred after cool-down conditions with low $dT/dz$ and high $B_a$, leading to significant flux trapping. Figure 3 shows an example of the difference between the temperature map measured at 2.0 K, 129 mT after cool-down with such conditions and the T-map measured during the baseline test at the same He bath temperature and rf field, for cavity PJ1-1. Additional hotspots occurred mainly in the high surface magnetic field region of the cavity due to the magnetic flux trapping during cool-down.

Both cavities were limited by quench. The quench location was different after each cool-down, suggesting that the quench was induced by trapped flux. The rf field was ramped up to the quench and ramped down to ~ 15 mT multiple times during each high-power rf test at 2 K to detect any hysteretic behavior. The results showed that any changes in the $Q_0(B_p)$-curves were well within the experimental uncertainty, however the temperature maps often showed hysteretic $\Delta T(B_p)$ at the quench location. The occurrence of other hotspots with hysteretic $\Delta T(B_p)$ was less common. Figure 4A shows an example of a hysteretic $\Delta T(B_p)$ at the quench location 200°/4 of cavity PJ1-1 after cool-down with low $dT/dz$ and high $B_a$, along with the $\Delta T(B_p)$ measured at the same location in the rf test after cool-down with high $dT/dz$ and low $B_a$. In the latter, the cavity quenched at a different location and no hysteretic behavior was measured. Figure 4B shows the $\Delta T(B_p)$ for the hotspot at location 60°/8 of cavity PJ1-1 after cool-down in opposite conditions, showing additional heating due to trapped flux following the cool-down with low $dT/dz$ and high $B_a$. The hysteretic temperature maps are consistent with hotspots caused by trapped magnetic flux.

The macroscopic size of the crystalline grains in cavity PJ1-1 allowed us to determine whether the hotspots are located at grain boundaries. We found that only 8 out of 49 hotspots were located on grain boundaries. A similar weak correlation between the hotspots locations and grain boundaries was reported in Ref. (Ciovati et al., 2007).

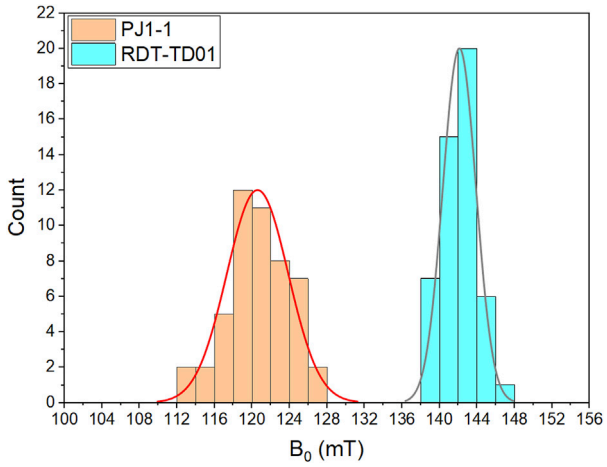


FIGURE 6
Distribution of the onset field, $B_0$, for the HFQS from 49 hotspots for cavities PJ1-1 (LG, BCP) and RDT-TD01 (FG, EP). Solid lines represent normal distributions for each cavity.

### 2.1.2 Hotspots analysis

The HFQS appears as a fairly sharp decrease of $Q_0(B_p)$, as shown in Figure 1. In order to determine the distribution of the local field onsets of the HFQS over the cavity surface, we analyzed 49 hotspots with maximum $\Delta T$ ranging from ≃ 40 mK to ≃ 400 mK measured on cavities PJ1-1 and RDT-TD01 during the baseline test. For each hotspot, the surface rf magnetic field corresponding to the onset of the local HFQS, $B_0$, was calculated from the intersection of least-squares linear fits of $\ln(\Delta T)$ vs. $\ln(B_{th})$ at low and high rf field, as shown in Figure 5. Here $B_{th}$ is the amplitude of the rf surface magnetic field at the thermometer location, given by the distribution of the magnetic field on the cavity inner surface calculated with a two-dimensional electromagnetic field solver Superfish (Billen and Young, 1996). For $B_{th} < B_0$, a quadratic dependence of the $\Delta T$ vs. $B_{th}$ is observed: this is consistent with Joule heating without anomalous rf losses. Figure 6 shows histograms of $B_0$ for these two cavities, both being consistent with a normal distribution following Shapiro-Wilks test, with a mean values of 121 mT and 142 mT for PJ1-1 and RDT-TD01, respectively, and standard deviations of 3.3 mT and 1.8 mT for PJ1-1 and RDT-TD01, respectively.

## 2.2 Results of magnetic field mapping

After completion of the rf tests the end-flanges were disassembled from cavity PJ1-1 and the cavity was degreased, high-pressure water rinsed, the end-flanges with fixed input and pick-up antennas were re-assembled back to the cavity. The cavity was then evacuated to ~ $10^{-8}$ mbar, leak-checked and isolated from the pumping system. The cavity was mounted to the test stand and a magnetic field scanning system (MFSS) was assembled to the cavity. The MFSS, described in details in Ref. (Parajuli et al., 2022), consists of two arms, 180° apart, one with 8 single-axis cryogenic Hall probes and one with 16 single-axis anisotropic magnetoresistance (AMR) sensors (Parajuli et al., 2021). The two arms are mounted on a rotating gear system, operated by a stepper motor outside the

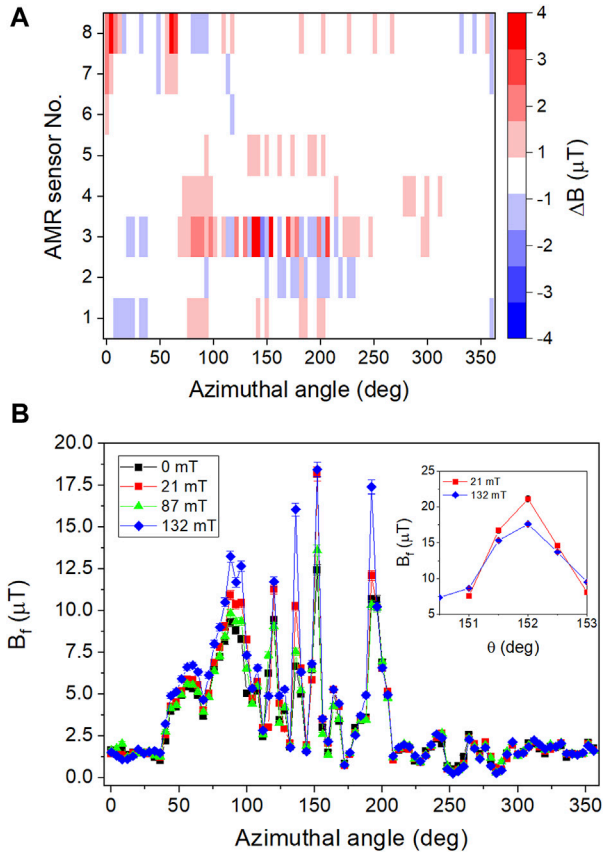


FIGURE 7
**(A)** Difference between $B_f$ measured at 132 mT minus $B_f$ measured with no rf field, both at 2.0 **(K)** **(B)** $B_f(\theta)$ measured by sensor No. 3 at different $B_p$-values. The inset in **(B)** shows a finer resolution scan of the peak at 150°.

cryostat, allowing full azimuthal coverage of the cavity surface. The arms with the magnetic field sensors have the same profile as the cavity and the sensors are distributed over the equator area of the cavity, where high rf magnetic field is present on the inner surface. The system was designed to measure the local magnetic field produced by bundles of vortices trapped within the cavity walls, therefore the sensors are positioned as close as possible to the cavity outer surface to measure the magnetic field component normal to the surface. The magnetic field component tangential to the surface is also measured by 8 out of 16 AMR sensors, next to the ones measuring the normal component. The magnetic field generated outside a superconductor by a trapped vortex is that of a magnetic monopole, which has zero azimuthal field component.

Two Cernox® RTDs were mounted on the top beam tube and two at the bottom beam tube, the distance between the two pairs being ~ 120 mm. The dc magnetic field applied along the cavity axis was produced by a set of Helmholts coils, 32 cm in diameter. Three single-axis FGMs were used to measure the applied field. Two sensors aligned along the cavity axis were taped on the top and bottom beam tube and one sensor measured the azimuthal component of the applied field at ~ 6 cm from the cavity equator.

After inserting the test stand into the cryostat, the experimental procedure consists of: (i) reset of the AMR sensors' magnetization by

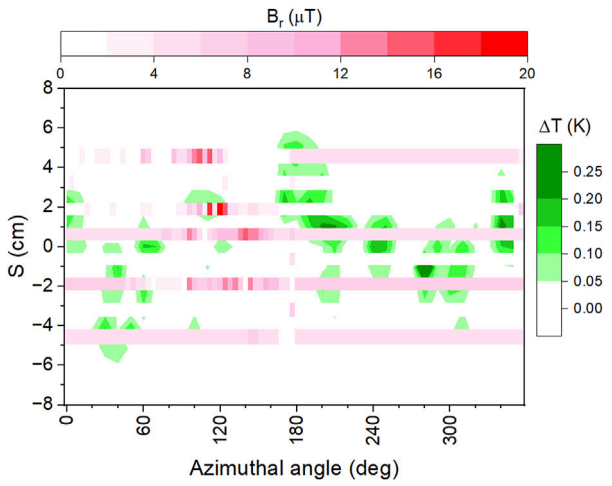


FIGURE 8
Overlay between unfolded temperature maps and magnetic field map with Hall probes, both measured at 2 K and $B_p$ = 136 mT, after cool-down in similar conditions. The variable $S$ is the distance from the equator along the cavity profile. Positive $S$-values are above the equator. The width of the B-map with the 8 Hall probes is not to scale.

applying a current pulse at room temperature, in low ambient field, $B_a \sim 0.5\ \mu$T; (ii) cool-down to ~ 10 K and measure the offset voltages of the magnetic field sensors; (iii) apply an axial dc magnetic field and cool-down through $T_c$ with either a high or low axial temperature gradient; (iv) fill the cryostat with LHe at 4.3 K and measure $Q_0(T, \sim 12\ \text{mT})$ during LHe pump-down to 1.6 K; (v) maintain the He bath temperature at 2.0 K and measure the trapped magnetic field on the cavity surface, with no rf field; (vi) measure $Q_0(B_p)$ at 2 K up to $B_{p,max}$ and back to ~ 10 mT, acquiring magnetic field maps at ≃ 21 mT, ≃ 82 mT and ≃ 132 mT. This measurement sequence was repeated for multiple cool-down conditions and $B_a$-values.

Figure 7A shows the difference, $\Delta B = B_f(\mathbf{r}, B_p) - B_f(\mathbf{r}, 0)$, between the magnitude of the local dc magnetic field $B_f(\mathbf{r}) = \sqrt{B_r^2 + B_t^2}$ at 2 K measured by AMR sensors at $B_p$ = 132 mT and the local field $B_f(\mathbf{r}, 0)$ at $B_p = 0$ and the same temperature during the test after cool-down with $dT/dz \sim 0.23$ K/cm and $B_a \sim 6.9\ \mu$T. Here $B_r$ and $B_t$ are the magnetic field components normal and tangential to the surface, respectively. Figure 7B shows $B_f$ measured by AMR sensor No. 3 during the same test, for different $B_p$-values. We observed that the average magnetic flux was nearly independent of $B_p$ in most cases, indicating that no new vortices penetrate in the cavity during rf tests. Yet we observed a local redistribution of the magnetic flux at some locations after applying the rf field, as shown in Figure 7 (Parajuli, 2022).

We investigated a possible correlations between the locations of flux spots revealed by magnetic field scanning and hotspots observed by temperature mapping. Figure 8 shows an example of an overlay between a temperature map at 2 K and $B_p$ = 136 mT and a magnetic field map measured by Hall probes at the same temperature and rf field, after cool-down with high $dT/dz$ and low $B_a$. It should be noted that the area sampled by a thermometer during T-mapping is ~ 4 × 6 mm$^2$, whereas the area sampled by a Hall-probe is 50 × 50 $\mu$m$^2$ and that micron-size defects at the inner cavity surface could produce millimeter-size hotspots on the outer surface at high rf fields (Gurevich and Ciovati, 2013). With these limitations in mind, no strong correlation was found between hotspots causing the HFQS and trapped flux spots.

## 3 Discussion

In spite of differences in the cavities surface preparation and treatment history, Figure 1A shows that their HFQS behavior is fairly similar. The totality of experimental data presented in Section 2 showed a remarkable difference in the magneto-thermal limitations of Nb cavities. On the one hand, cavities with the HFQS remain thermally stable even when dissipating $P_c \sim 200$ W at 2 K. In such conditions the average power density ~ 0.24 W/cm$^2$ is still below the threshold for film boiling at 2 K, even though the temperature of the outer cavity surface locally exceeds $T_\lambda = 2.17$ K at some hotspots. When the same cavities were tested with the T-mapping system installed, they quenched at a lower $P_c$. This indicates that the array of thermometers being in contact with the outer cavity surface reduces the surface area cooled by liquid He by ~ 15%, facilitating the premature quench. The change in the quench locations observed during tests with T-mapping and the hysteretic behavior of $\Delta T(B_p)$ at the quench locations suggest that trapped vortices may contribute to the quench. On the other hand, cavities may quench with $P_c < 10$ W and $\Delta T < 10$ mK at the breakdown field (Lechner et al., 2023). Quenching of such cavities likely has a magnetic field origin related to the behavior of the nonlinear BCS surface resistance at high rf fields.

The above results pose the following questions: (i) What can result in the sharp downturn of $Q(B_p)$ at $B_p \approx 120$ mT? (ii) Why do the cavities with the extended HFQS remain thermally stable even if they dissipate more than ten times than the cavities without the HFQS at the breakdown field? For instance, some cavities quench with no overheating and very low total dissipated power while others they can sustain 200 W without quench, even though $R_s(B_{p,max})/R_s(0) \sim 30$. (iii) What mechanisms determine the magnitude of the HFQS and the breakdown field?

To address these questions, we use a thermal feedback model (Gurevich, 2012) in which $T(B_p)$ at the inner cavity surface is determined by the balance of rf power and cooling power of heat transfer through the cavity wall:

$$\frac{B_p^2}{2\mu_0^2}\left[R_{BCS}(T) + R_i\left(B_p\right)\right] = \frac{h_K \kappa (T - T_0)}{\kappa + d h_K}. \tag{1}$$

Here $h_K$ is the Kapitza thermal conductance and $\kappa$ is the thermal conductivity taken at the temperature of the coolant $T_0$, $d$ is the thickness of the cavity wall. For the sake of simplicity we assume that Eq. 1 describes an averaged temperature $T(B_p)$, $R_{BCS}(T)$ is independent of $B_p$ and $R_i(B_p)$ is independent of $T$:

$$R_{BCS}(T) = \frac{\mu_0^2 \omega^2 \lambda^3 \Delta}{\rho_n k_B T} \ln\left(\frac{9 k_B T}{4\hbar\omega}\right) e^{-\Delta/k_B T}, \tag{2}$$

$$R_i\left(B_p\right) = R_1 + R_2\left[1 + \tanh\left(\frac{B_p - B_0}{B_1}\right)\right]. \tag{3}$$

Here we use $R_{BCS}(T)$ in the dirty limit (Gurevich, 2012) and adopt a phenomenological model in which the residual surface

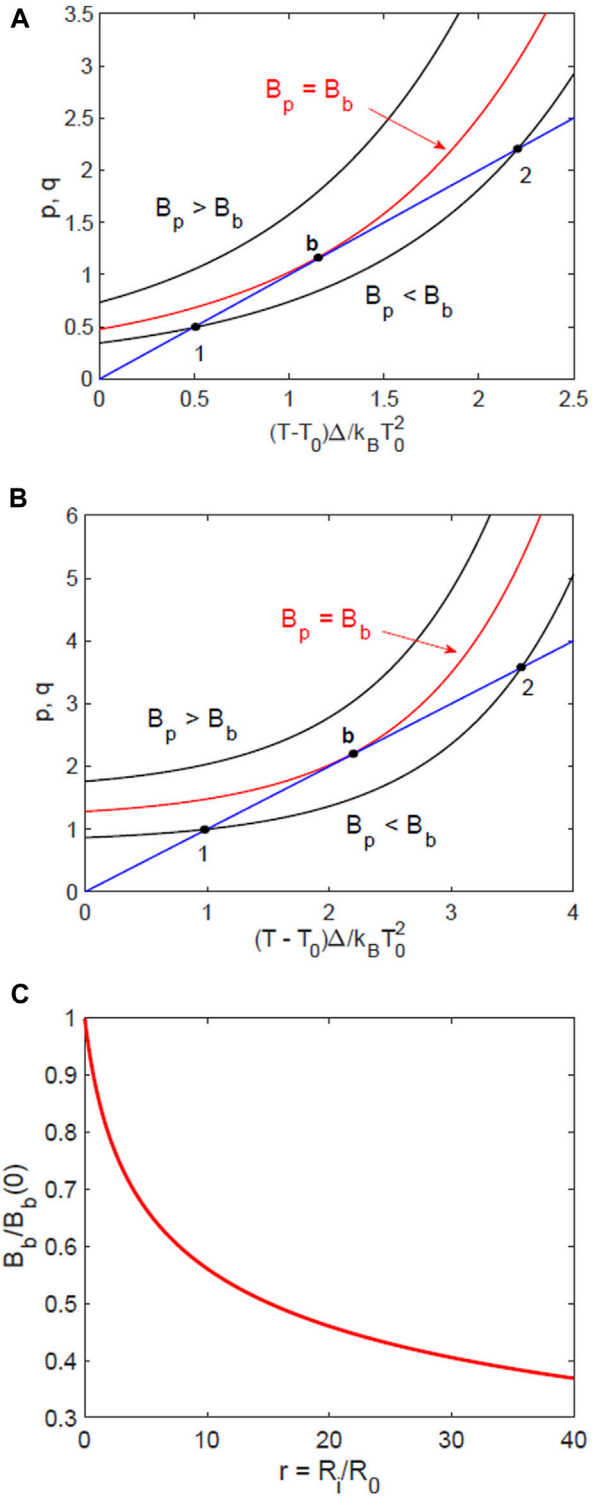


FIGURE 9
Graphic solution of the heat balance Eqs 1–3 for: **(A)** $R_i = 0.2R_0$ and **(B)** $R_i = 10R_0$. The blue line shows the dimensionless cooling power $q = \theta$ in the r.h.s. of Eq. 4 and the black and red curves show the rf power $p$ in the l.h.s. of Eq. 4 at different fields. The points 1 and 2 correspond to stable and unstable uniform states, respectively. **(C)** The decrease of the thermal breakdown field $B_b$ with $R_i$.

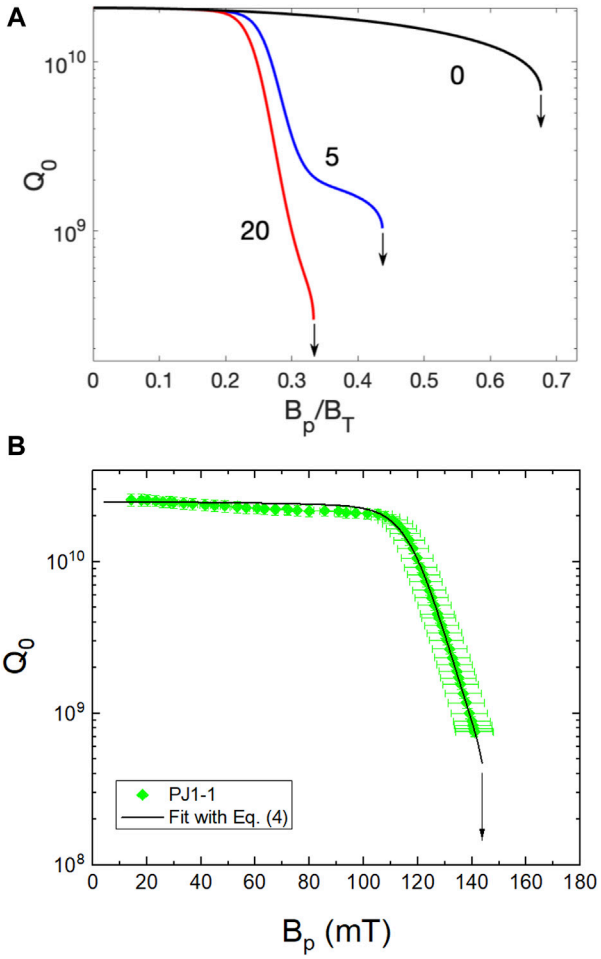


FIGURE 10
**(A)** $Q_0(B_p)$ calculated for a field-induced transition at $B_0 = 0.3B_T$ with $B_1 = 0.1B_0$, $R_1 = 0.2R_0$ and $k_BT_0/\Delta = 1/9$. The numbers by the curves show $R_2$ in units of $R_0$. The black curve shows $Q_0(B_p)$ without the field-induced transition, where $Q_0$ at $B_p = 0$ was set to $2.5 \times 10^{10}$. The arrows at the end points of $Q_0(B_p)$ depict the thermal quench. **(B)** $Q_0(B_p)$ measured at 2 K for cavity PJ1-1 without temperature mapping, shown in Figure 1A, and least-squares fit with Eq. 4 for $B_0 = 142.4$ mT, $B_1 = 12.3$ mT, $R_2 = 33.6R_0$ and $R_1 = 0.35R_0$. The arrow represents the quench field predicted by the model.

resistance $R_i$ $(B_p)$ has a transition from a low-resistance state $R_i \approx R_1$ at $B_p \lesssim B_0$ to a high-resistance state with $R_i \approx R_1 + 2R_2$ at $B_p \gtrsim B_0$. Mechanisms of the transition field $B_0$ and the broadening parameter $B_1$ are discussed later. It is convenient to write Eq. 1 in the dimensionless form

$$b^2\left[r(b) + \exp\left[\theta/(1+t_0\theta)\right]/(1+t_0\theta)\right] = \theta, \tag{4}$$

where $\theta = (T - T_0)\Delta/k_BT_0^2$, $t_0 = k_BT_0/\Delta$, $b = B_p/B_T$, $B_T = [2\mu_0^2\kappa h_K k_B T_0^2/\Delta(\kappa + dh_K)R_0]^{1/2}$, $r = R_i/R_0$, a slow temperature dependence of the logarithmic factor in Eq. 2 is neglected, and $R_0 = R_{BCS}(T_0)$.

We solved Eqs 1–3 numerically to calculate $T(B_p)$ and the surface resistance $R_s[B_p, T(B_p)]$ affected by the parameters $B_0$, $B_1$

and $R_2$ of the resistive transition. Graphic solutions of Eq. 4 shown in Figure 9 give an insight into the greater thermal stability of the HFQS state. At $B_p$ below a thermal breakdown field $B_b$, there are two stationary temperature states $T_1$ and $T_2$: a stable state 1 and an unstable state 2. The existence of the unstable state 2 implies that the state 1 is metastable with respect to a heat pulse causing the overheating larger than $T_2 - T_1$ and igniting a thermal quench. The points 1 and 2 merge at a thermal breakdown field $B_b$ above which no stable states exist because the cooling power cannot balance the RF power.

The thermal breakdown of superconductivity is primarily driven by the strong increase of $R_{BCS}(T)$ with $T$ resulting in thermal runaway at $B_p = B_b$ at a critical overheating $T_b - T_0$ much smaller than either $T_c$ and $T_0$. For instance, at $R_i \ll R_0$ the thermal runaway occurs at a rather weak overheating $T_b - T_0 = k_B T_0^2/\Delta \simeq 0.22$ K at $T_0 = 2$ K and $\Delta = 18$ K (Gurevich, 2012). In this case $Q(B_p)$ decreases gradually with $B_p$ down to $Q(B_b) \approx 0.37Q(0)$ without any HFQS. At $R_i \ll R_0$ the thermal quench field in Nb cavities at 2 K and 1–2 GHz exceeds the superheating field $B_s$ so the overheating is secondary and the superconductivity breaks down due to the instability of the Meissner state caused by rf currents. However, as $R_i$ increases, the thermal breakdown field $B_b$ decreases below $B_s$, while the critical overheating $T_b - T_0$ increases from $T_b - T_0 = 0.22$ K at $R_i = 0$ to $T_b - T_0 \simeq 0.45$ K at $R_i = 10R_0$, as shown in Figures 9B, C. It is the extra dissipation caused by the residual resistance and the increase of $T_b - T_0$ with $R_i$ which produce the HFQS. Indeed, a constant $R_i$ increases $T_1 - T_0$ but does not cause the thermal quench which requires a strong increase of $R_{BCS}(T)$ with $T$, as characteristic of thermally-bistable systems (Gurevich and Mints, 1987). At small $R_i < R_0$ the critical overheating $T_b - T_0$ increases linearly with $R_i$ while $B_b$ decreases linearly with $R_i$ (Gurevich and Ciovati, 2013):

$$T_b - T_0 = \frac{k_B T_0^2}{\Delta}\left[1 + \frac{R_i}{eR_0}\right], \tag{5}$$

$$B_b = \left[\frac{2\mu_0^2 \kappa h_K k_B T_0^2}{e\Delta(\kappa + dh_K)R_0}\right]^{1/2}\left[1 - \frac{R_i}{2eR_0}\right], \tag{6}$$

where $e = 2.718$. Figure 10A shows the evolution of $Q_0(B_p)$ as the magnitude $2R_2$ of the resistive step in $R_i(B_p)$ increases. In all cases the thermal quench occurs at the end points of the $Q_0(B_p)$ curves. The HFQS state followed by quench is clearly visible at $R_2 = 20R_0$. At a smaller $R_2 = 5R_0$ the model predicts a partial HFQS followed by the flattening of $Q_0(B_p)$ before quench. Figure 10B shows that this thermal feedback model with $B_0 = 142.4$ mT, $B_1 = 12.3$ mT and $R_2 = 33.6R_0$ fits our HFQS experimental data quite well. Here $R_1 = 0.35R_0$ was obtained from a least-squares fit of $R_s(T)$ at low rf field, and the thermal quench occurs at $B_b = 143$ mT, beyond the last datapoint in Figure 10B. Therefore, the resistive transition in $R_i(B_p)$ does not eliminate the thermal quench but increases stable overheating causing an extended decrease of $Q_0(B_p)$ with $B_p$ and a significant increase of the rf power before the thermal breakdown at $B_p = B_b$. In what follows we discuss possible mechanisms of the stepwise increase of $R_i(B_p)$.

The experimental results presented in Section 2 show that: (i) the hotspots distribution is not affected strongly by the magnitude of a temperature gradient applied during cool-down; (ii) additional hotspots are produced by trapped magnetic flux, resulting from an ambient field $\gtrsim 4$ $\mu$T during cool-down, but the overheating starts at low rf field and it is less steep, with increasing rf field, than what is measured in the HFQS region; (iii) no strong correlation was found between trapped flux locations and hotspots associated with the HFQS, after cool-down with conditions which minimize the amount of trapped flux. Even though an earlier study showed that some HFQS hotspots may be attributed to trapped vortices (Ciovati and Gurevich, 2008), our experimental data indicate that trapped vortices are hardly a dominant cause of the HFQS in the cavities studied in this work.

The above conclusion is consistent with numerical simulations of trapped vortices perpendicular to the surface and interacting with randomly distributed pinning centers (Pathirana and Gurevich, 2020; Pathirana and Gurevich, 2021). In this case $R_i(B_p)$ increases with $B_p$ at low fields and levels off above a depinning field $B_d$ which depends on the elementary pinning forces, pin density and rf frequency. Although the rf depinning of trapped vortices can produce a stepwise increase of $R_i(B_p)$ at $B_p \gtrsim B_d$ (Dhakal et al., 2020; Pathirana and Gurevich, 2020; Pathirana and Gurevich, 2021), it can hardly explain the observed features of HFQS at $B_0 \simeq 120$–$160$ mT. First, the depinning field $B_p \lesssim 0.1$–$0.3B_{c1} \sim 10$–$40$ mT obtained in numerical simulations is well below $B_0$ even for strong pins (like 10–20 nm oxide or hydride precipitates). Second, the calculated width of the rf depinning transition $\simeq B_p$ is much wider than the observed sharp transition to the HFQS state with the width $\lesssim 0.1B_0$. Such broadening of the depinning transition results from random distribution of pinning centers and strong variations of the pin spacings from the cavity surface.

The HFQS may also be attributed to the presence of normal-conducting nano-precipitates within the rf penetration depth. These nano-precipitates are superconducting at low rf field due to the proximity effect and become normal above a threshold field, related to the onset of the HFQS. Such nano-precipitates can be niobium hydrides (Romanenko et al., 2013a) or metallic suboxides (Weingarten, 2011). Hydride precipitates caused by excessive hydrogen can nucleate on crystal defects, such as vacancies and low-angle grain boundaries (Sung et al., 2017). Evidence of nanohydrides within a $\sim 1$ $\mu$m depth from the Nb surface was found by transmission electron microscopy (TEM) on cavity cutout samples (Trenikhina et al., 2015) as well as combined scanning TEM and atom-probe tomography on flat, high-purity Nb samples after standard surface treatments (Kim et al., 2013). Some evidence for nanohydrides on the surface of cavity cutout samples was recently reported (Sung et al., 2023). The reduction of the HFQS after LTB was correlated to the lower volume fraction of hydrides (Trenikhina et al., 2015) which was, in turn, related to fewer vacancies (Wenskat et al., 2020). It was found that a slow cool-down at temperatures 90–150 K facilitates the formation of lossy hydrides (Knobloch, 2003), which can be a mix of $\epsilon$, $\beta$ and $\zeta$ phases, according to the phase diagram of Nb-H (Welter and Johnen, 1977). One may expect that larger volume fraction of hydrides resulting from holding a cavity in this temperature region for several hours would reduce the onset of the HFQS or increase the intensity or the number of hotspots (Barkov et al., 2013). However, we observed no such correlation, as was reported in Section 2.

A field dependence of $R_s(B_p)$, based on a distribution of precipitates with different sizes, was proposed in Ref.

(Romanenko et al., 2013a). The model of Ref. (Weingarten, 2011). invokes the presence of NbO nano-precipitates at the Nb surface but several TEM studies of the Nb surface revealed a uniform, layered oxide structure with no evidence of NbO nano-precipitates (Batchelor et al., 2007; Tao et al., 2011; Sung et al., 2014; Trenikhina et al., 2015). Another possibility of the HFQS involves penetration of mixed Abrikosov-Josephson (AJ) vortices (Gurevich, 2002; Sheikhzada and Gurevich, 2017) along a network of strongly coupled grain boundaries in a polycrystalline Nb. All these scenarios have one common feature inconsistent with the observed sharp downturn of $Q_0(B_p)$ at the onset of the HFQS with a narrow transition width $B_1 \simeq (8–9)\%B_0$ shown in Figure 1. Indeed, a random distribution of nano-precipitates would produce a broader transition to a HFQS, not only because of different sizes and shapes of nanoprecipitates but also because the superconductivity breakdown of the $i$th precipitate spaced by $L_i$ from the surface occurs at the applied field $B_0 \sim (J_{ci}\lambda/\mu_0)\exp(L_i/\lambda)$, where $J_{ci}$ is a shape-dependent critical current density causing the breakdown. Hence, random local spacings of precipitates from the surface can produce an exponentially broad distribution of local transition fields manifesting themselves in a broad HFQS. The same argument is applicable to a broad distribution of local penetration fields of AJ vortices along grain boundaries with different Josephson currents and random orientation with respect to the surface. Those materials broadening mechanisms are augmented by a "natural" width of the HFQS transition due to a lateral variation of the rf field at the cavity equatorial surface for the $TM_{010}$ mode.

A mechanism which could account for the observed sharp HFQS transition may be related to the breakdown of proximity induced superconductivity at $B_p = B_0$ in the metallic suboxide layer of thickness $d \simeq 1$ nm (Sun et al., 2023). Such suboxide layer is directly exposed to the rf field, so the transition occurs at a well-defined field without exponential broadening due to a random distribution of $L_i$. Yet because the surface rf field varies along the cavity surface, the breakdown of superconductivity in the suboxide layer would first occur at the equator and then spread over the surface as $B_p$ is increased. In this case the resistive transition in the global $R_i(B_p)$ would be broadened over an intrinsic width $B_1$ depending on the cavity geometry and the excited resonant mode.

To see if the above mechanism could produce the step in $R_i(B_0)$ accounting for the HFQS shown in Figure 10B, we evaluate the extra rf power $P_i$ in a suboxide overlayer of thickness $d$ as it becomes normal at $B_p > B_0$. Here $P_i$ is controlled by the electric field $E = \omega B\lambda$ at the cavity surface, $P_i = d\sigma_i E^2/2 = d\sigma_i \omega^2 B_p^2 \lambda^2/2$, resulting in the residual resistance at $B_p \gtrsim B_0 + B_1$:

$$R_i = d\sigma_i \omega^2 \mu_0^2 \lambda^2, \tag{7}$$

where $\sigma_i$ is the normal conductivity of the overlayer. The ratio $r = R_i/R_{BCS}$ defined by Eqs 2, 7 is then:

$$r = \frac{d\sigma_i k_B T \exp(\Delta/k_B T)}{\lambda\sigma_n \Delta \ln(9k_B T/4\hbar\omega)}. \tag{8}$$

Taking here $\Delta/k_B T = 9$ at 2 K, $d/\lambda = 0.025–0.05$, $\sigma_i = \sigma_n$ and $9k_B T/4\hbar\omega = 47$ at 2 GHz, gives $r \approx 6–12$. Moreover, the broadening of the DOS peaks reduces the factor $\ln(9k_B T/4\hbar\omega)$ in Eq. 8 to $\ln(k_B T/\Gamma)$, where $\Gamma$ is the Dynes parameter (Gurevich, 2023). For $\Gamma \simeq 10^{-2}\Delta$ (Lechner et al., 2020), we get $k_B T/\Gamma \simeq 11$, so that $R_{BCS}$ is reduced by a factor $\simeq 1.61$ and the ratio $r$ increases to $r \simeq 10–20$. In turn, the breakdown of the proximity coupled superconductivity in the suboxide causes superconductivity suppression in an adjacent surface layer of Nb (Kubo and Gurevich, 2019), further increasing the thickness of the dissipative layer at the surface. As a result, the breakdown of proximity-induced superconductivity in the suboxide may significantly increase $R_i$ $(B_p)$ at $B_p > B_0$, giving rise to the HFQS.

Microscopic calculations of the breakdown field $B_{sn}$ of a proximity-coupled thick normal overlayer with $d_i \gtrsim \xi_n$ show that $B_{sn}$ can be well below the superheating field $B_s$ (Fauchére and Blatter, 1997). However for thin ($d_i \ll \xi_n$) suboxide overlayers characteristic of Nb surface, $B_{sn}$ is of the order of $B_s$ but the actual value of $B_{sn}$ depends strongly on such materials-sensitive parameters as $\sigma_i$, $d_i$ and the interface contact resistance between the N layer and the bulk Nb (Kubo and Gurevich, 2019). A thin proximity-coupled suboxide layer not only reduces the field onset of HFQS but also causes a slight decrease in $\Delta$ affecting $R_{BCS}(T)$. A correlation between the reduction of $B_0$ and $\Delta$ was observed in Ref. (Ciovati et al., 2007).

## 4 Conclusion

The use of a variable coupler, along with a novel magnetic field scanning apparatus and the traditional temperature mapping setup provided valuable insights into the dissipative state of Nb cavities at high rf fields. We found that the location of hotspots causing the HFQS is reproducible upon thermal cycling through $T_c$, the intensity and location of hotspots causing the HFQS are not altered significantly after holding the cavity at temperatures which promote the formation of Nb hydrides. A narrow distribution of the onset field for the HFQS at different hotspot locations was observed, resulting in a sharp upturn of $R_s(B_p)$ above ~ 120 mT. These results are inconsistent with the HFQS being due to a random distribution of nano-precipitates within the rf penetration depth. The HFQS was found not to be impacted significantly by trapped magnetic flux and poor correlation was found between the location of hotspots causing the HFQS and trapped flux locations. Such findings suggest that trapped vortices are not a major source of the HFQS hotspots.

The remarkable thermal stability of some cavities with the HFQS can be explained by the thermal feedback model, incorporating a field-dependent residual resistance. The observed $Q_0(B_p)$ curves can be described well by a model in which the residual resistance has a sharp transition from a low-resistance state to a high-resistance state, above a threshold rf field. Such transition can result from suppression of the proximity effect-induced superconductivity in a thin metallic suboxide layer between the dielectric surface oxide and the bulk Nb by rf currents at strong fields $B_p \gtrsim B_0$. In this scenario the HFQS can result from surface treatments increasing the thickness of the suboxide layer or the interface boundary resistance $R_\square$, shifting the transition field $B_0$ below the thermal breakdown field $B_b$. Conversely, materials treatments such as the LTB which may shrink the suboxide layer and reduce $R_\square$, or change the

superconducting parameters at the surface in such a way that the ratio $r$ in Eq. 8 is decreased, would either diminish the HFQS or eliminate it completely if $B_0 > B_b$.

## Data availability statement

The raw data supporting the conclusions of this article will be made available by the authors, without undue reservation.

## Author contributions

IP: Data curation, Formal Analysis, Investigation, Software, Writing–review and editing. GC: Conceptualization, Data curation, Formal Analysis, Funding acquisition, Methodology, Resources, Supervision, Writing–original draft, Writing–review and editing. AG: Formal Analysis, Funding acquisition, Writing–original draft, Writing–review and editing.

## Funding

The author(s) declare financial support was received for the research, authorship, and/or publication of this article. The work of AG and IP was supported by NSF under grant PHY 100614-010 and by DOE under grant SC10087-20. GC is supported by Jefferson Science Associates, LLC under U.S. DOE Contract No. DE-AC05-06OR23177.

## Acknowledgments

We would like to acknowledge P. Dhakal, R. Geng, G. Eremeev, and A. Palczewski for providing some of the cavities used for this study and the SRF Cavity Production Group at Jefferson Lab for helping with some of the cavity preparation and cool-down.

## Conflict of interest

The authors declare that the research was conducted in the absence of any commercial or financial relationships that could be construed as a potential conflict of interest.

## Publisher's note



## Supplementary material

The Supplementary Material for this article can be found online at: https://www.frontiersin.org/articles/10.3389/femat.2024.1339293/full#supplementary-material

## References

Antoine, C. (2012). Materials and surface aspects in the development of SRF Niobium cavities. *EuCARD Editor. Ser. Accel. Sci. Technol.* 12. EuCARD-BOO-2012-001

Aune, B., Bandelmann, R., Bloess, D., Bonin, B., Bosotti, A., Champion, M., et al. (2000). Superconducting TESLA cavities. *Phys. Rev. St. Accel. Beams* 3, 092001. doi:10.1103/physrevstab.3.092001

Barkov, F., Romanenko, A., Trenikhina, Y., and Grassellino, A. (2013). Precipitation of hydrides in high purity niobium after different treatments. *J. Appl. Phys.* 114, 164904. doi:10.1063/1.4826901

Batchelor, A. D., Leonard, D. N., Russell, P. E., Stevie, F. A., Griffis, D. P., and Myneni, G. R. (2007). TEM and SIMS analysis of (100), (110), and (111) single crystal niobium. *AIP Conf. Proc.* 927, 72. doi:10.1063/1.2770680

Billen, J. H., and Young, L. M. (1996). Poisson SUPERFISH, *tech. Rep. LA-UR-96-1834*. Los Alamos, NM, United States: Los Alamos National Laboratory. revised February 6, 2003.

Bonin, B., and Röth, R. W. (1992). "Q-degradation of niobium cavities due to hydrogen contamination," in *Proceedings of the 5th workshop on RF superconductivity, hamburg, Germany, 1991*. Editor D. Proch (Hamburg, Germany: DESY), 210–244.

Charrier, J. P., Coadou, B., and Visentin, B. (2019). "Improvements of superconducting cavity performances at high accelerating gradients," in *Proc. EPAC'98* (Geneva, Switzerland: JACoW Publishing), 1185–1887.

Ciovati, G. (2004). Effect of low-temperature baking on the radio-frequency properties of niobium superconducting cavities for particle accelerators. *J. Appl. Phys.* 96, 1591–1600. doi:10.1063/1.1767295

Ciovati, G. (2005). *Investigation of the superconducting properties of niobium radio-frequency cavities* (United States: Old Dominion University). Ph.D. thesis.

Ciovati, G. (2006a). "Review of the frontier workshop and Q-slope results, Physica C: superconductivity," in proceedings of the 12th International Workshop on RF Superconductivity 441, Ithaca, NY, USA, 10 - 15 July 2005, 44.

Ciovati, G. (2006b). Improved oxygen diffusion model to explain the effect of low-temperature baking on high field losses in niobium superconducting cavities. *Appl. Phys. Lett.* 89, 022507. doi:10.1063/1.2220059

Ciovati, G., Eremeev, G., and Hannon, F. (2018). High field $q$ slope and the effect of low-temperature baking at 3 ghz. *Phys. Rev. Accel. Beams* 21, 012002. doi:10.1103/physrevaccelbeams.21.012002

Ciovati, G., and Gurevich, A. (2008). Evidence of high-field radio-frequency hot spots due to trapped vortices in niobium cavities. *Phys. Rev. St. Accel. Beams* 11, 122001. doi:10.1103/physrevstab.11.122001

Ciovati, G., and Kneisel, P. (2006). Measurement of the high-field $Q$ drop in the $TM_{010}$ and $TE_{011}$ modes in a niobium cavity. *Phys. Rev. St. Accel. Beams* 9, 042001. doi:10.1103/physrevstab.9.042001

Ciovati, G., Kneisel, P., and Gurevich, A. (2007). Measurement of the high-field $Q$ drop in a high-purity large-grain niobium cavity for different oxidation processes. *Phys. Rev. St. Accel. Beams* 10, 062002. doi:10.1103/physrevstab.10.062002

Ciovati, G., Myneni, G., Stevie, F., Maheshwari, P., and Griffis, D. (2010). High field $Q$ slope and the baking effect: review of recent experimental results and new data on Nb heat treatments. *Phys. Rev. St. Accel. Beams* 13, 022002. doi:10.1103/physrevstab.13.022002

Ciovati, G., and Turlington, L. (2019). "A simple variable coupler for the cryogenic test of SRF cavities," in *Proc. SRF'19* (Geneva, Switzerland: JACoW Publishing), 282–284.

Dhakal, P., Ciovati, G., and Gurevich, A. (2020). Flux expulsion in niobium superconducting radio-frequency cavities of different purity and essential contributions to the flux sensitivity. *Phys. Rev. Accel. Beams* 23, 023102. doi:10.1103/physrevaccelbeams.23.023102

Eremeev, G., Padamsee, H., Liepe, M., and Roy, R. (2013). "Effect of mild baking on high field Q-drop of BCP cavity," in *Proc. SRF'03* (Geneva, Switzerland: JACoW Publishing), 70–73.

Eremeev, G., and Palczewski, A. D. (2014). Characterization of superconducting radiofrequency breakdown by two-mode excitation. *J. Appl. Phys.* 115, 023901. doi:10.1063/1.4861396

Eremeev, G. V., and Padamsee, H. (2006). "A comparison of large grain and fine grain cavities using thermometry," in *Proc. EPAC'06* (Geneva, Switzerland: JACoW Publishing), 475–477.

Fauchére, A. L., and Blatter, G. (1997). Magnetic breakdown in a normal-metal–superconductor proximity sandwich. *Phys. Rev. B* 56, 14102–14107. doi:10.1103/physrevb.56.14102

Geng, R. L., Dai, J., Eremeev, G. V., and Palczewski, A. D. (2011). "Progress of ILC high gradient SRF cavity R&D at Jefferson Lab," in *Proc. IPAC'11* (Geneva, Switzerland: JACoW Publishing), 334–336.

Gurevich, A. (2002). Nonlinear dynamics of vortices in easy flow channels along grain boundaries in superconductors. *Phys. Rev. B* 65, 214531. doi:10.1103/physrevb.65.214531

Gurevich, A. (2012). Superconducting radio-frequency fundamentals for particle accelerators. *Rev. Acceler. Sci. Technol.* 5, 119–146. doi:10.1142/s1793626812300058

Gurevich, A. (2023). Tuning microwave losses in superconducting resonators. *Supercond. Sci. Technol.* 36, 063002. doi:10.1088/1361-6668/acc214

Gurevich, A., and Ciovati, G. (2013). Effect of vortex hotspots on the radio-frequency surface resistance of superconductors. *Phys. Rev. B* 87, 054502. doi:10.1103/physrevb.87.054502

Gurevich, A. V., and Mints, R. (1987). Self heating in normal metals and superconductors. *Rev. Mod. Phys.* 59, 941–999. doi:10.1103/revmodphys.59.941

Halbritter, J. (1978). On electric surface impedance. *Z. Phys. B* 31, 19–37. doi:10.1007/bf01320123

Huang, S., Kubo, T., and Geng, R. L. (2016). Dependence of trapped-flux-induced surface resistance of a large-grain nb superconducting radio-frequency cavity on spatial temperature gradient during cooldown through $T_c$. *Phys. Rev. Accel. Beams* 19, 082001. doi:10.1103/physrevaccelbeams.19.082001

Kim, Y.-J., Tao, R., Klie, R. F., and Seidman, D. N. (2013). Direct atomic-scale imaging of hydrogen and oxygen interstitials in pure niobium using atom-probe tomography and aberration-corrected scanning transmission electron microscopy. *ACS Nano* 7, 732–739. doi:10.1021/nn305029b

Kneisel, P., Ciovati, G., Dhakal, P., Saito, K., Singer, W., Singer, X., et al. (2015). Review of ingot niobium as a material for superconducting radiofrequency accelerating cavities. *Nucl. Instrum. Methods Phys. Res. Sect. A Accel. Spectrom. Detect. Assoc. Equip.* 774, 133–150. doi:10.1016/j.nima.2014.11.083

Knobloch, J. (1997). *Advanced thermometry studies of superconducting radio-frequency cavities* (United States: Cornell University). Ph.D. thesis.

Knobloch, J. (2003). The "Q disease" in superconducting niobium RF cavities. *AIP Conf. Proc.* 671, 133. doi:10.1063/1.1597364

Knobloch, J., Muller, H., and Padamsee, H. (1994). Design of a high speed, high resolution thermometry system for 1.5 GHz superconducting radio frequency cavities. *Rev. Sci. Instrum.* 65, 3521–3527. doi:10.1063/1.1144532

Kubo, T., and Gurevich, A. (2019). Field-dependent nonlinear surface resistance and its optimization by surface nano-structuring in superconductors. *Phys. Rev. B* 100, 064522. doi:10.1103/physrevb.100.064522

Lechner, E. M., Oli, B. D., Makita, J., Ciovati, G., Gurevich, A., and Iavarone, M. (2020). Electron tunneling and x-ray photoelectron spectroscopy studies of the superconducting properties of nitrogen-doped niobium resonator cavities. *Phys. Rev. Appl.* 13, 044044. doi:10.1103/physrevapplied.13.044044

Lechner, E. M., Oli, B. D., Makita, J., Ciovati, G., Gurevich, A., and Iavarone, M. (2023). Characterization of dissipative regions of a n-doped superconducting radio-frequency cavity. *Front. Electron. Mater.* 3. doi:10.3389/femat.2023.1235918

Liarte, D. B., Hall, D., Koufalis, P. N., Miyazaki, A., Senanian, A., Liepe, M., et al. (2018). Vortex dynamics and losses due to pinning: dissipation from trapped magnetic flux in resonant superconducting radio-frequency cavities. *Phys. Rev. Appl.* 10, 054057. doi:10.1103/physrevapplied.10.054057

Padamsee, H. (2001). The science and technology of superconducting cavities for accelerators. *Supercond. Sci. Technol.* 14, R28–R51. doi:10.1088/0953-2048/14/4/202

Padamsee, H. (2009). "Residual losses from trapped dc magnetic flux," in *RF superconductivity: Science, technology, and applications* (Weinheim, Germany: WILEY-VCH Verlag), 69–70.

Padamsee, H., Proch, D., Kneisel, P., and Mioduszewski, J. (1981). Field strength limitations in superconducting cavities-multipacting and thermal breakdown. *IEEE Trans. Magnetics* 17, 947–950. doi:10.1109/tmag.1981.1061065

Parajuli, I. (2022). *Characterization of losses in superconducting radio-frequency cavities by combined temperature and magnetic field mapping* (United States: Old Dominion University). Ph.D. thesis.

Parajuli, I., Ciovati, G., and Delayen, J. R. (2022). High resolution diagnostic tools for superconducting radio frequency cavities. *Rev. Sci. Instrum.* 93, 113305. doi:10.1063/5.0117868

Parajuli, I. P., Ciovati, G., and Delayen, J. R. (2021). Magnetic field sensors for detection of trapped flux in superconducting radio frequency cavities. *Rev. Sci. Instrum.* 92, 104705. doi:10.1063/5.0063177

Pathirana, W. P. M. R., and Gurevich, A. (2020). Nonlinear dynamics and dissipation of a curvilinear vortex driven by a strong time-dependent meissner current. *Phys. Rev. B* 101, 064504. doi:10.1103/physrevb.101.064504

Pathirana, W. P. M. R., and Gurevich, A. (2021). Effect of random pinning on nonlinear dynamics and dissipation of a vortex driven by a strong microwave current. *Phys. Rev. B* 103, 184518. doi:10.1103/physrevb.103.184518

Posen, S., Checchin, M., Crawford, A., Grassellino, A., Martinello, M., Melnychuk, O., et al. (2016). Efficient expulsion of magnetic flux in superconducting radiofrequency cavities for high $Q_0$ applications. *J. Appl. Phys.* 119, 213903. doi:10.1063/1.4953087

Posen, S., Cravatta, A., Checchin, M., Aderhold, S., Adolphsen, C., Arkan, T., et al. (2022). High gradient performance and quench behavior of a verification cryomodule for a high energy continuous wave linear accelerator. *Phys. Rev. Accel. Beams* 25, 042001. doi:10.1103/physrevaccelbeams.25.042001

Reece, C., Almeida, B., Powers, T., and Susta, J. (1991). "A closed cycle cryogenic system for testing superconducting RF cavities," in *Proc. PAC'91* (Geneva, Switzerland: JACoW Publishing), 2325–2328.

Romanenko, A., Barkov, F., Cooley, L. D., and Grassellino, A. (2013a). Proximity breakdown of hydrides in superconducting niobium cavities. *Supercond. Sci. Technol.* 26, 035003. doi:10.1088/0953-2048/26/3/035003

Romanenko, A., Grassellino, A., Barkov, F., and Ozelis, J. P. (2013b). Effect of mild baking on superconducting niobium cavities investigated by sequential nanoremoval. *Phys. Rev. St. Accel. Beams* 16, 012001. doi:10.1103/physrevstab.16.012001

Romanenko, A., Grassellino, A., Crawford, A., Sergatskov, D., and Melnychuk, O. (2014). Ultra-high quality factors in superconducting niobium cavities in ambient magnetic fields up to 190 mg. *Appl. Phys. Lett.* 105, 234103. doi:10.1063/1.4903808

Romijn, R., Weingarten, W., and Piel, H. (1983). Calibration of the scanning thermometer resistor system for a superconducting accelerating cavity. *IEEE Trans. Magn.* 19, 1318–1321. doi:10.1109/tmag.1983.1062425

Sheikhzada, A., and Gurevich, A. (2017). Dynamic transition of vortices into phase slips and generation of vortex-antivortex pairs in thin film josephson junctions under dc and ac currents. *Phys. Rev. B* 95, 214507. doi:10.1103/physrevb.95.214507

Shu, Q. S., Möller, W.-D., Pekeler, M., Proch, D., Junquera, T., and Fouaidy, M. (1996). "Experimental investigation of quenches in superfluid He of TESLA 9-cell superconducting cavities," in *Proc. SRF'95* (Geneva, Switzerland: JACoW Publishing), 431–435.

Sun, Z., Baraissov, Z., Dukes, C. A., Dare, D. K., Oseroff, T., Thompson, M. O., et al. (2023). Surface oxides, carbides, and impurities on rf superconducting Nb and Nb3Sn: a comprehensive analysis. *Supercond. Sci. Technol.* 36, 115030. doi:10.1088/1361-6668/acff23

Sung, Z. H., Cano, A., Murthy, A., Karapetrova, E., Lee, J., Martinello, M., et al. (2023). First direct observation of nanometer size hydride precipitations on superconducting niobium. arXiv:2305.01022 [cond-mat.mtrl-sci] Available at: https://arxiv.org/abs/2305.01022.

Sung, Z.-H., Lee, P. J., and Larbalestier, D. C. (2014). Observation of the microstructure of grain boundary oxides in superconducting rf-quality niobium with high-resolution TEM (transmission electron microscope). *IEEE Trans. Appl. Supercond.* 24, 68–73. doi:10.1109/tasc.2013.2287050

Sung, Z. H., Wang, M., Polyanskii, A. A., Santosh, C., Balachandran, S., Compton, C., et al. (2017). Development of low angle grain boundaries in lightly deformed superconducting niobium and their influence on hydride distribution and flux perturbation. *J. Appl. Phys.* 121. doi:10.1063/1.4983512

Tao, R., Todorovic, R., Liu, J., Meyer, R. J., Arnold, A., Walkosz, W., et al. (2011). Electron energy-loss spectroscopy study of metallic Nb and Nb oxides. *J. Appl. Phys.* 110, 124313. doi:10.1063/1.3665193

Trenikhina, Y., Romanenko, A., Kwon, J., Zuo, J.-M., and Zasadzinski, J. F. (2015). Nanostructural features degrading the performance of superconducting radio frequency niobium cavities revealed by transmission electron microscopy and electron energy loss spectroscopy. *J. Appl. Phys.* 117, 154507. doi:10.1063/1.4918272

Visentin, B. (2003). "Q-slope at high gradients: review of experiments and theories," in *Proc. SRF'03* (Geneva, Switzerland: JACoW Publishing), 199–205.

Visentin, B. (2006). "Review on Q-drop mechanisms," in International Workshop on Thin Films and New Ideas for Pushing the Limits of RF Superconductivity, Legnaro, Padua, Italy, 9-12 October 2006.

Visentin, B., Charrier, J. P., Coadou, B., and Roudier, D. (1999). "Cavity baking: a cure for the high accelerator field $Q_0$ drop," in *Proc. SRF'99* (Geneva, Switzerland: JACoW Publishing), 198–202.

Vogt, J.-M., Kugeler, O., and Knobloch, J. (2013). Impact of cool-down conditions at $T_c$ on the superconducting rf cavity quality factor. *Phys. Rev. Special Topics-Accelerators Beams* 16, 102002. doi:10.1103/physrevstab.16.102002

Weingarten, W. (2011). Field-dependent surface resistance for superconducting niobium accelerating cavities. *Phys. Rev. St. Accel. Beams* 14, 101002. doi:10.1103/physrevstab.14.101002

Welter, J. -M., and Johnen, F. J. (1977). Superconducting transition temperature and low temperature resistivity in the niobium-hydrogen system. *Z. für Phys. B Condens. Matter* 27, 227–232. doi:10.1007/bf01325532

Wenskat, M., Čižek, J., Liedke, M. O., Butterling, M., Bate, C., Haušild, P., et al. (2020). Vacancy-hydrogen interaction in niobium during low-temperature baking. *Sci. Rep.* 10, 8300. doi:10.1038/s41598-020-65083-0

Xie, Y., and Liepe, M. (2013). "New insights into quench caused by surface pits in SRF cavities," in *Proc. SRF'13* (Geneva, Switzerland: JACoW Publishing), 378–391.